



Synthesis of novel ruthenium II phenanthroline complex and its application to TiO₂ and ZnO nanoparticles on the electrode of dye sensitized solar cells



Sule Erten-Ela^{a,*}, Selcan Sogut^b, Kasim Ocakoglu^{b,**}

^a Solar Energy Institute, Ege University, Bornova, 35100 Izmir, Turkey

^b Advanced Technology Research & Application Center, Mersin University, Ciftlikkoy Campus, TR-33343 Yenisehir, Mersin, Turkey

ARTICLE INFO

Available online 19 March 2014

Keywords:

Ruthenium

Dye sensitized solar cell

Thin film

Nanocrystalline TiO₂ and ZnO

ABSTRACT

Novel ruthenium (II) phenanthroline complex, Ru^{II}(4,4',4''-tri-tert-butyl-2,2':6',2''-terpyridine)-(4,7-diphenyl-1,10-phenanthroline-disulfonic acid disodium salt)(thiocyanate), [Ru(L1)(L2)(NCS)], [K328] was designed and synthesized as a photosensitizer for the dye sensitized solar cells (DSSCs) using TiO₂ and ZnO electrodes. The density functional theory (DFT) calculation was used to estimate the photovoltaic properties of the complex in the design stage. In this paper, our aim was to investigate the interaction between semiconductor and anchoring groups like sulfonate group that binds onto TiO₂ and ZnO surface. The influence of the semiconductor type on the performance of TiO₂ and ZnO based photovoltaics has been tested. The solar cell performance of TiO₂ based solar cell shows better efficiencies compared to ZnO based solar cell. Although sulfonate group did offer stronger binding onto the semiconductor surface, this does not help to improve cell performance for ZnO based solar cells.

© 2014 Elsevier Ltd. All rights reserved.

1. Introduction

A significant progress has been made in their performance and stability since invention of dye-sensitized solar cells (DSSCs) as a low cost next-generation solar cell [1]. Nanocrystalline TiO₂, a well-known metaloxide semiconductor, has been widely studied for numerous applications [2–5]. Photosensitization of porous nanocrystalline TiO₂ film electrodes using ruthenium complexes has intensively been investigated for solar cell applications. Recently, the effects of the number of anchoring carboxyl groups on the solar cell performance of ruthenium phenanthroline

complexes have been reported [6–11]. The molecular structure of the sensitizer has a critical role on the solar cell performance, and therefore, this effect has been examined in detail in this study. The chemistry of 1,10-phenanthroline complexes of ruthenium is often very similar to that of corresponding 2,2'-bipyridyl complexes [12,13]. Phenanthroline, however, is structurally more rigid and symmetrical. In this context, the most efficient sensitizers studied so far are some ruthenium complexes which can be chemisorbed on the TiO₂ surface via the carboxylate group [14,15]. Alternative anchoring groups are the phosphonic and sulfonic acids that bind even more strongly onto TiO₂. Grafting sensitizers on the surface of TiO₂ with the phosphonic acid group has been reported earlier [16–20]. We previously reported that the number of anchoring carboxyl groups affects the solar cell performance of dye sensitized nanocrystalline TiO₂ solar cells using ruthenium complexes [6]. Hence, it is of great

* Corresponding author. Tel.: +90 232 3111231; fax: +90 232 3886027.

** Corresponding author.

E-mail addresses: suleerten@yahoo.com,

sule.erten@ege.edu.tr (S. Erten-Ela), kasimocakoglu@gmail.com,

kasim.ocakoglu@mersin.edu.tr (K. Ocakoglu).

interest to design and synthesize ruthenium sensitizers bearing the sulfonate groups for dye sensitized solar cells. In this paper we report on the synthesis and photophysical and photoelectrochemical behaviors of such sensitizers. We show that such a rational sensitizer design enables good photovoltaic performances to be matched with very strong surface binding. For this purpose, a novel ruthenium complex containing phenanthroline ligand with bulky sulfonate and tert-butyl groups, [Ru^{II}(4,4',4''-tri-tert-butyl-2,2':6',2''-terpyridine)-(4,7-diphenyl-1,10-phenanthroline-disulfonic acid disodium salt)(thiocyanate)], [Ru(L1)(L2)(NCS)], [K328] was synthesized, and examined theoretically by the DFT technique. The DFT calculations are used to investigate the vertical excitation energies, corresponding excitation wavelengths and oscillator strengths, predominant orbitals involved in 10 singlet–singlet transitions and their characters obtained from the single point TD-DFT calculations for K328.

2. Experimental

All materials are of reagent grade and are used as received unless otherwise noted.

2.1. Materials

All organic solvents are purchased from Merck and Fluka, and used as received. [RuCl₂(*p*-cymene)]₂, 4,4',4''-tri-tert-butyl-2,2':6',2''-terpyridine (L1), 4,7-diphenyl-1,10-phenanthroline-disulfonic acid disodium salt (L2), NH₄SCN and Sephadex LH-20 are purchased from Aldrich.

2.2. Characterization

The UV–vis absorption spectra of synthesized dyes are recorded in a 1 cm path length quartz cell by using an Analytic JENA S 600. The infrared (IR) spectra are obtained by using a Perkin-Elmer, FT-IR/MIR-FIR (ATR) spectrophotometer. ¹H NMR spectra are measured on a Bruker 400 MHz spectrometer. Cyclic voltammetry measurements of synthesized dye are taken by using a CH-Instrument 660 B Model Potentiostat equipment. Thermal stabilities are determined by means of thermal gravimetric measurements (TGA) with an equipment of Perkin-Elmer, Thermogravimetric Analyzer Pyris 6 TGA. Dye sensitized solar cells are characterized by current–voltage (*J*–*V*) measurements. All current–voltage (*J*–*V*) measurements are done under 100 mW/cm² light intensity and AM 1.5 conditions. A 450 W Xenon light source (Oriol) is used to give an irradiance of various intensities. *J*–*V* data collection is made by using a Keithley 2400 Source-Meter and LabView data acquisition software.

2.3. Synthesis of dyes and precursor compounds

All commercially available chemicals and solvents are used without further purification. Synthetic details and characterization of ruthenium complexes are described below. The molecular structure of ruthenium complex and ground state optimization are shown in Fig. 1.

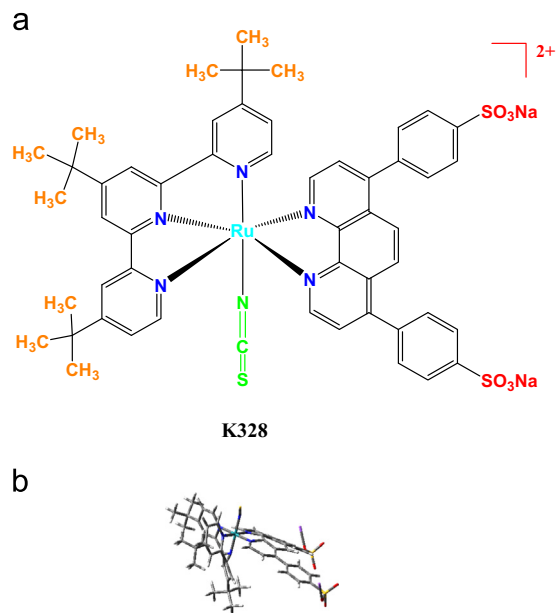


Fig. 1. Structures of ruthenium(II) complex (a) and ground state optimization of K328 at B3LYP/LANL2DZ_OPT_FREQ (b).

2.3.1. Synthesis of Ru^{II}(4,4',4''-tri-tert-butyl-2,2':6',2''-terpyridine)-(4,7-diphenyl-1,10-phenanthroline-disulfonic acid disodium salt)(thiocyanate), [Ru(L1)(L2)(NCS)], [K328]

[RuCl₂(*p*-cymene)]₂ (0.1 g, 0.16 mmol) and 4,4',4''-tri-tert-butyl-2,2':6',2''-terpyridine (L1) (0.1311 g, 0.32 mmol) are taken in a Schlenk tube and dissolved in dry DMF (30 mL). The reaction mixture is heated to 60 °C in an inert atmosphere for 4 h with constant stirring. Subsequently, 4,7-diphenyl-1,10-phenanthroline-disulfonic acid disodium salt (L2) (0.1928 g, 0.32 mmol) is added to this reaction flask and the reaction mixture is heated in dark at 150 °C for 4 h. Finally, an excess amount of NH₄NCS (50 mg, 0.656 mmol) is added to the reaction mixture and the heating continued for another 4 h. The reaction mixture is cooled to room temperature and the solvent is removed by using a rotary evaporator under vacuum. The solid is extracted with methanol, filtered and dried in vacuum. On a Sephadex LH-20 column the crude complex is purified with methanol as an eluent; 297 mg, 80% yield. Anal. Calc. for RuC₅₂H₄₉N₆Na₂O₆S₃Cl₂: C, 53.47; H, 4.23; N, 7.19. Found: C, 53.44; H, 4.21; N, 7.18%. FT-IR (ATR, cm⁻¹): 3419, 3132, 3043, 2961, 2866, 2099, 2050, 2045, 1609, 1405, 1172, 1124, 1030, 801, 745, 739, 727, 701. ¹H NMR (CD₃OD) δ (ppm): 8.90 (br s, 2H, NCHCH), 8.70 (br s, 2H, NCHCH), 8.30–8.15 (m, 2H, NCHCHC), 8.13–7.95 (m, 6H, C(CH₃)₃CH), 7.86 (br s, 1H, CCHCHC), 7.80 (br s, 1H, CCHCHC), 7.57 (br s, 2H, CHCSO₃Na), 7.50 (br s, 2H, CHCSO₃Na), 7.45–7.15 (m, 4H, CCHCHCH), 1.71 (s, 9H, CCH₃), 1.34 (s, 18H, CCH₃).

2.4. Electrochemical, absorption and emission studies

The redox potentials of the complex are measured using a three-electrode apparatus comprising a platinum wire counter-electrode, working electrode, and an Ag/AgCl

reference electrode. CH_2Cl_2 is used as a solvent and the supporting electrolyte is tetrabutylammonium hexafluorophosphate (TBAPF_6), 0.1 M. Ferrocene is added to each sample solution at the end of the experiments and ferrocenium/ferrocene redox couple is used as an internal potential reference.

2.5. Photovoltaic characterization

2.5.1. Fabrication of TiO_2 and ZnO based DSSCs and characterization

Depositions of nanostructured TiO_2 and ZnO films on the FTO glasses were achieved by the doctor blading technique with $4\ \mu\text{m}$ thicknesses. TiO_2 and ZnO pastes were prepared in ethanol. The pastes were stored with stirring and ultrasonically agitated for 1 h before film depositions. The films were generally white and opaque in appearance. After sintering, the substrates were immersed in a 0.5 mM solution of the ruthenium dye complexes in DMF at room temperature overnight, and dried under a flow of nitrogen. The active solar cell areas of TiO_2 and ZnO cells were $0.16\ \text{cm}^2$. Pt catalyst was deposited on the FTO glasses by coating with a drop of H_2PtCl_6 solution with heat treatment at $450\ ^\circ\text{C}$ for 15 min. The dye covered TiO_2 and ZnO electrodes and Pt-counter-electrode were assembled into a sandwich type cell. The cells were sealed using a Surlyn ($60\ \mu\text{m}$, Solaronix) and 0.6 M N-methyl-N-butyl-imidazolium iodide (BMII)+0.1 M LiI+0.05 M I_2 +0.5 M 4-tert-butylpyridine (TBP) in acetonitrile as redox electrolyte solution was introduced through pre-drilled holes in the counter-electrode. The filling holes were sealed using Surlyn and a microscope cover glass. Current-voltage (J - V) curves were obtained using the Keithley measurement unit and the light source consisted of an Oriol Xe-lamp. Schematic drawings of TiO_2 and ZnO based dye sensitized solar cells are shown in Fig. 2.

3. Results and discussion

3.1. Photophysical property of dye

The absorption and emission maxima of the complex measured in MeOH solution are summarized in Table 1. The normalized absorption and emission spectra are displayed in Fig. 3. The complex showed broad absorption bands in the 270–500 nm region. The two high-energy bands at 277 and 312 nm for K328 arise due to intraligand π - π^* transitions. The lower energy part of the absorption spectra of the complex is dominated by MLCT transitions with maxima at 446 and 495 nm. A red-shift of about 10 nm is observed for the lowest energy MLCT band of K328. The low energy MLCT absorption band at 495 nm of the complex has a molar extinction coefficient of $2.0 \times 10^4\ \text{L/mol cm}$, which is higher than the corresponding value for Z-907 ($1.2 \times 10^4\ \text{L/mol cm}$). The emission data of the dye is obtained in an air-equilibrated MeOH solution at 298 K by exciting in the respective low energy MLCT absorption band, showing an emission maximum at 700 nm.

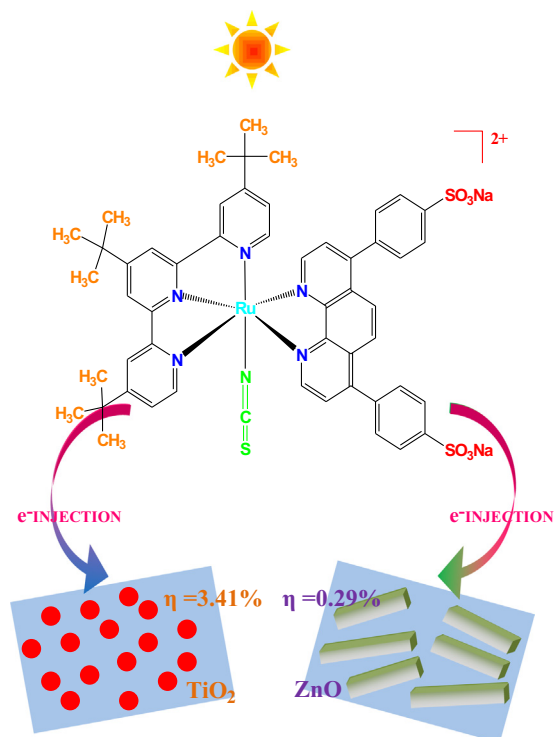


Fig. 2. Schematic drawing of TiO_2 and ZnO based dye sensitized solar cells.

Table 1

UV-vis absorption and emission properties of ruthenium complex measured in MeOH.

	λ_{max} (nm) ($\epsilon/10^4\ \text{M}^{-1}\ \text{cm}^{-1}$)		Emission λ_{max} (nm)
	L (π - π^*)	4d- π^*	
K328	277 (7.56), 312 (4.76)	446 (1.67), 495 (2.02)	700

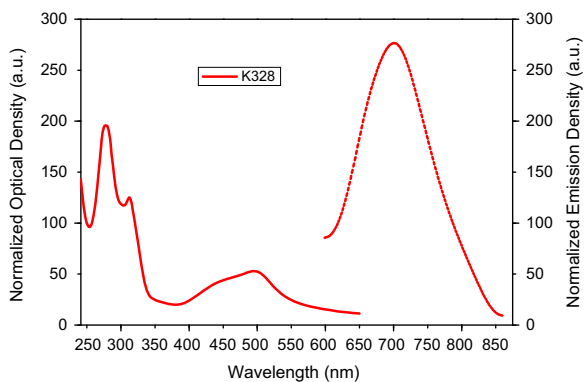


Fig. 3. UV-vis absorption (solid lines) and steady-state fluorescence spectra (dashed lines) of K328 measured in MeOH; λ_{ex} : 450 nm for K328.

3.2. Thermal analyses of dye

The thermogravimetric analysis (TGA) of the prepared complex was measured in the range 50 – $800\ ^\circ\text{C}$ in order to

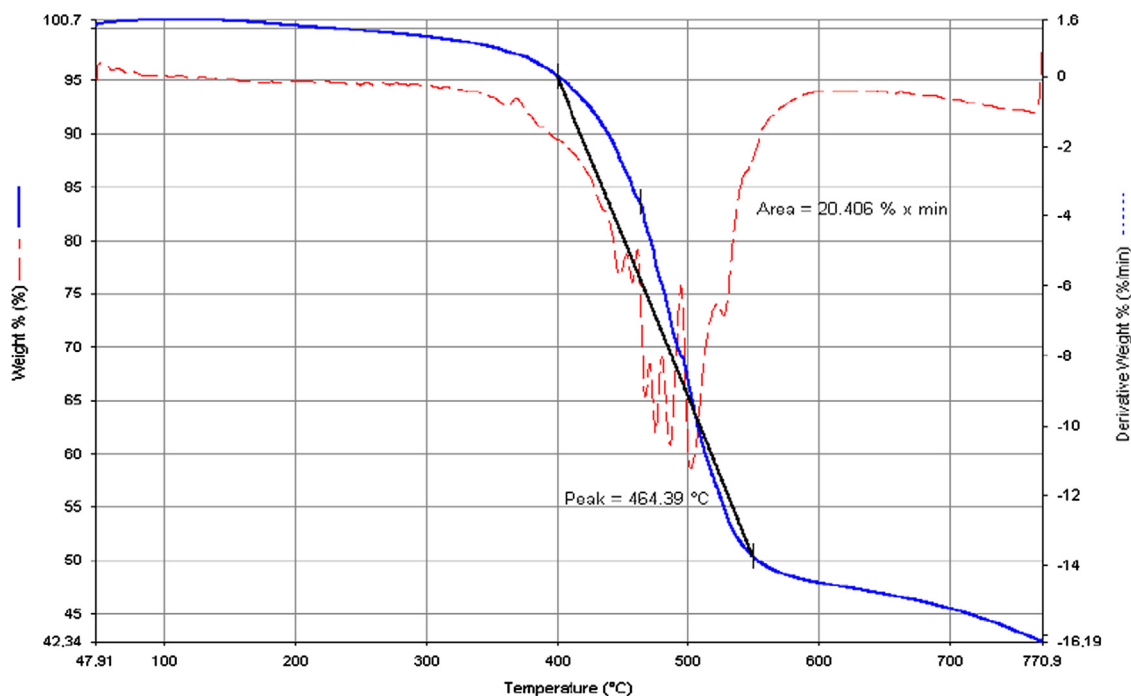


Fig. 4. The thermogravimetric analyses (TGA) of K328.

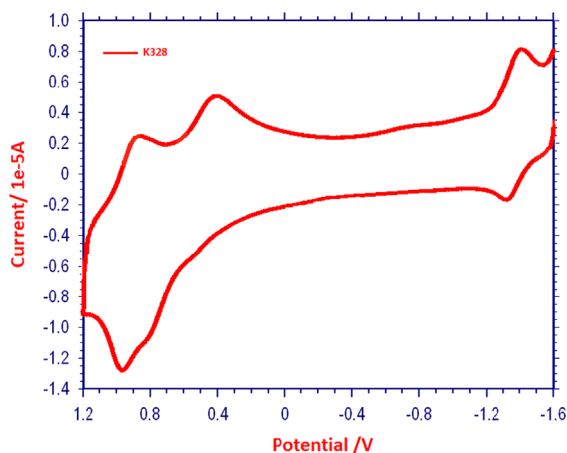


Fig. 5. Cyclic voltammogram of ruthenium complex K328.

investigate the thermal stability. According to TG traces shown in Fig. 4, the degradation starts with breaking of the methyl groups of the ligand L1. The weight losses of the complex at 500 and 800 °C are 35% and 58%, respectively. As seen from Fig. 4, the degradation process is not complete up to 800 °C, and the high percentage of the residues at this temperature most probably comes from metal oxide (sodium and ruthenium).

3.3. Electrochemical properties of dye

Cyclic voltammetry (CV) measurements of the ruthenium complex were performed in CH_2Cl_2 with 0.1 M

Table 2

Redox potentials and E_{HOMO} and E_{LUMO} levels of ruthenium complex.

	$E_{\text{oxidation}}^a$ (V)	$E_{\text{reduction}}^b$ (V)	$E_{\text{ferrocene}}^c$ (V)	E_{HOMO}^d (eV)	E_{LUMO}^e (eV)	$E_{\text{band gap}}^f$
K328	0.69	-1.36	0.46	5.03	2.98	2.05

^a First oxidation potentials of Ru complex.

^b Reduction potentials of Ru complex.

^c Potentials of ferrocene, internal reference electrode.

^d HOMO energy level of Ru complex.

^e LUMO energy level of Ru complex.

^f Energy band gap of Ru complex.

tetrabutylammonium hexafluorophosphate (TBAPF₆), to evaluate the electron transfer possibility from excited state of the dye to the conduction bands of TiO₂ and ZnO (Fig. 5). The ruthenium complex shows reversible reduction and oxidation processes, and the redox potentials and calculated E_{HOMO} and E_{LUMO} energy levels are given in Table 2. Ferrocene was used as an internal standard for calibrating. The oxidation potential observed at 0.69 V (vs Ag/AgCl reference electrode) can be assigned to the oxidation of metal center. The first oxidation potential of ruthenium complex is more positive than that of the I^-/I_3^- redox couple (~ 0.4 V vs NHE), providing a thermodynamic driving force for an efficient dye regeneration by iodide. The reduction peak of the complex is observed at -1.36 V. The electrochemical measurement of complex shows that electron injection process is energetically favorable. The E_{LUMO} levels are suitable for an electron injection into the conduction band of TiO₂ and ZnO. Experimental and calculated energy levels are presented in Fig. 6.

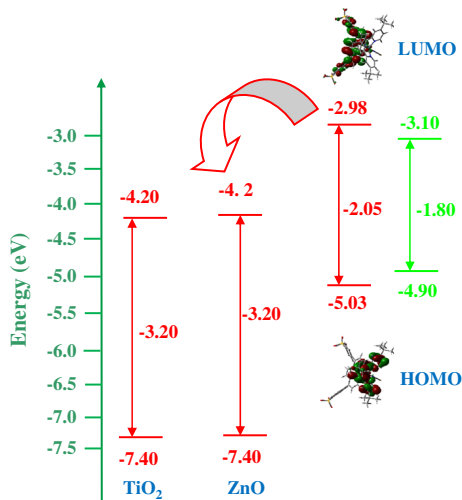


Fig. 6. Schematic representation of frontier orbitals of K328, along with isodensity plots of HOMO and LUMO orbitals. The experimental and calculated energy levels are displayed in solid and dashed line, respectively.

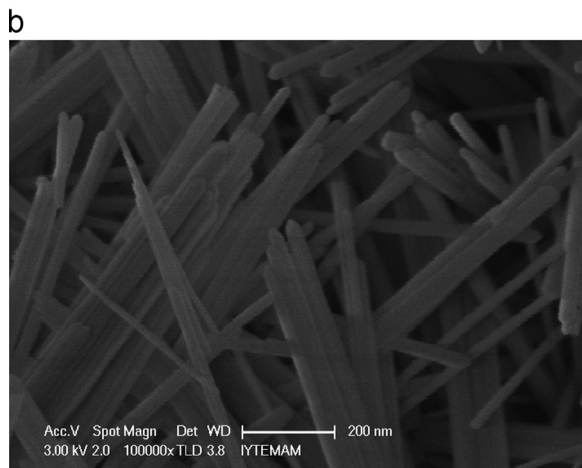
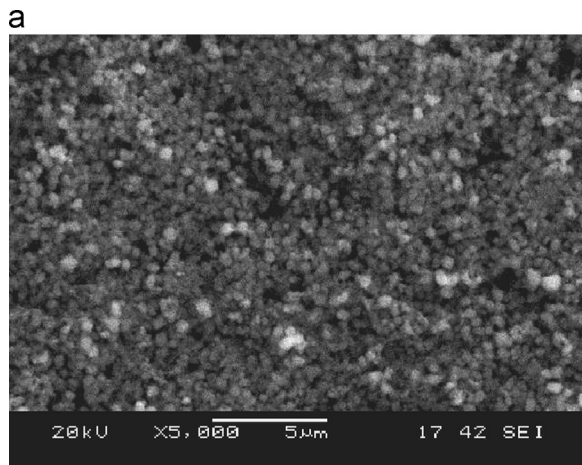


Fig. 7. Scanning electron microscopy (SEM) image of TiO₂ nanoparticles (a) and ZnO nanorods (b).

3.4. Synthesis and characterization of ZnO nanorods

ZnO nanorods are synthesized according to the following procedure. In a typical experiment, zinc acetate is dissolved in 25 ml deionized water in a beaker. The concentration of zinc acetate dihydrate is 0.55 M. The solution is stirred with a magnetic bar at 100 °C for 1 h until a transparent mixture is obtained. Subsequently, the solution is loaded into a 500 mL Teflon-lined stainless steel autoclave, which is then sealed and maintained at 200 °C for 36 h. The autoclave is cooled to room temperature, and the mixture is poured into a beaker. After the water evaporation at 200 °C, the wet precipitate is dried in an oven at 90 °C for 12 h. The lengths and diameters of ZnO nanorods are in the ranges 800–1100 nm and 18–27 nm, respectively. XRD patterns indicate that the peaks corresponding to the ZnO phase are quite prominent compared to the Zn-related peaks. The XRD measurement reveals the formation of ZnO nanorods with the use of calcination method. The diffraction peaks positioned at 2θ values 31.8°, 34.5°, 36.3°, 47.6°, 56.6°, 62.9°, 66.3°, 68.0°, 69.2°, 72.5°, and 76.9° can be indexed to the hexagonal wurtzite phase of zinc oxide (JCPDS card no. 36-1451) [21]. SEM image of the obtained ZnO nanorods is shown in Fig. 7.

3.5. Photovoltaic performance

The current–voltage curves for DSSCs based on ruthenium complex are compared in Fig. 8 and Table 3. Photovoltaic performances (J – V) of the ruthenium complex K328 using TiO₂ and ZnO electrodes are studied. Under standard global AM 1.5 solar irradiation, the TiO₂ solar cell sensitized with K328 gives a short-circuit current density (J_{sc}) of 10.82 mA cm⁻², open circuit voltage (V_{oc}) of 527 mV, and a

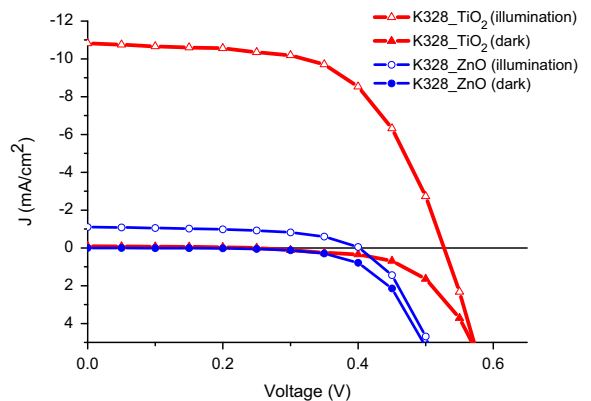


Fig. 8. Current density–voltage curves of TiO₂ and ZnO based dye sensitized solar cells.

Table 3

Photovoltaic performances of TiO₂ and ZnO based dye sensitized solar cells.

	J_{sc} (mA cm ⁻²)	V_{oc} (mV)	FF	η (%)
K328_TiO ₂	10.82	527	0.57	3.41
K328_ZnO	1.22	400	0.53	0.29

fill factor of 0.57, corresponding to an overall conversion efficiency (η) of 3.41%. Under the same conditions, ZnO based DSSC using K328 ruthenium complex exhibited J_{sc} : 1.22 mA cm⁻², V_{oc} : 400 mV and FF : 0.53 with an overall conversion efficiency of η : 0.26%.

Photocurrent performance of K328/ZnO solar cell is lower than that of K328/TiO₂ solar cell, whereas the amount of adsorbed ruthenium complex exceeds that on TiO₂ surface. Photovoltaic performance of the K328/ZnO solar cell does not show high efficiency compared to that of the K328/TiO₂ solar cell. Binding of the complex onto the semiconductor surfaces can take place only via sulfonate groups. According to reports in the literature, six different adsorption modes can be seen between dye and metal oxide surfaces [22,23]; (i) covalent bonding of dye onto the semiconductor surface, (ii) electrostatic interactions, (iii) hydrogen bonding, (iv) self-assembly, (v) physisorption of dye on the surface via van der Waals interactions, and (vi) physical entrapment [22,23]. For the complex K328, electrostatic interactions occurring between sulfonate anchoring group and semiconductor surface would be more dominant compared to the others. The binding ability of the dyes onto the semiconductor surface via negatively charged anchoring groups such as sulfonate strongly depends on pH of the solution which easily affects the surface charge of the semiconductor. Dye adsorption onto TiO₂ or ZnO surfaces via sulfonate groups has been monitored as a function of solution pH in numerous studies [24]. Hydroxyl groups bonded at the zinc oxide nanoparticle surface also play an important role in the surface charge equilibrium (positive or negative) of the semiconductor [25]. In this context, the electrostatic interactions taking place at the dye–semiconductor interface are very important. For instance, dodecylbenzenesulfonate molecules can easily bind through the sulfonate group (SO₃⁻) with the positively charged TiO₂ nanoparticles [26]. Although sulfonate group did offer stronger binding onto the semiconductor surface, this does not help improve cell performance for the ZnO based DSSC. This situation can be explained by the pH of the solution which affects the surface charge of the semiconductor. As a result of this effect, the complex binding onto the ZnO surface cannot contribute to electron injection efficiently, and this leads to lower electron injection yield for ZnO based DSSC compared to TiO₂ electrodes.

3.6. Density functional theory

All ground-state geometry optimization calculations are performed with the Gaussian 03 program package [27] employing the density functional theory (DFT) method with Becke's three parameters hybrid functional [28] and Lee–Yang–Parr's gradient corrected correlation functional (B3LYP) [29]. The LanL2DZ basis set [30] and effective core potential are used for the ruthenium atom basis set [31] and applied for all other atoms. In addition, in order to obtain the vertical excitation energies of the complexes, single point time dependent density functional theory (TD-DFT) [32] using B3LYP is utilized with the LANL2DZ basis set by using its ground state DFT geometries.

Table 4 gives the vertical excitation energies, corresponding excitation wavelengths and oscillator strengths, predominant orbitals involved in 10 singlet–singlet transitions and their characters obtained from the single point TD-DFT calculations for K328. The molecular orbital (MO) plots of the K328 molecule involving the lowest 10 energy CT transitions ($S_0 \rightarrow S_1$, $S_0 \rightarrow S_2$, $S_0 \rightarrow S_3$, $S_0 \rightarrow S_4$, $S_0 \rightarrow S_5$, $S_0 \rightarrow S_6$, $S_0 \rightarrow S_7$, $S_0 \rightarrow S_8$, $S_0 \rightarrow S_9$ and $S_0 \rightarrow S_{10}$) are displayed in Fig. 9. As clearly seen from Fig. 9, HOMOs are completely localized on the donor Ru[*tert-butyl-bpy*] groups and LUMOs are localized on the acceptor Ru[*phen*] groups and it is clear that the HOMO–LUMO transitions of K328 will have $\pi \rightarrow \pi^*$ character.

The TD-DFT calculations imply that the $S_0 \rightarrow S_1$ transition for the K328 complex cannot be observed in the UV/vis range since its oscillator strength is $f=0.0010$ at 1032.98 nm. On the other hand, the corresponding transition in the K328 complex has significant oscillator strength $S_0 \rightarrow S_1:0.0010$ and $S_0 \rightarrow S_{10}:0.0615$. The $S_0 \rightarrow S_2$ transitions with an excitation wavelength of 997 nm are also CT transitions. In the UV/vis range, the visibility of the $S_0 \rightarrow S_2$ transition seems highly improbable since it has oscillator strength of only 0.0012, leading to significant charge transfer transition.

The transitions having the largest five oscillator strengths (their excitation wavelengths in decreasing oscillator strength order are 810, 802, 746, 608, and 573 nm) belong to the charge transfer (CT). The transition possessing the largest oscillator strength of 0.1013 is a charge transfer of [Ru(*tert-butyl-bpy*)] \rightarrow Ru[*phen*] at 608.17 nm.

As a result, the computational study revealed that the complex has thermodynamic stability at the ground state in

Table 4
Calculated properties of electronically excited states of (K328).

State	ΔE (eV)	λ_{exc} (nm)	Oscillator strength (f)	Predominant transitions	Character
$S_0 \rightarrow S_1$	1.2003	1032.98	0.0010	(HOMO) \rightarrow (LUMO+1)	CT ^a (COOH–CO)
$S_0 \rightarrow S_2$	1.2424	997.97	0.0012	(HOMO) \rightarrow (LUMO)	CT (RuNCS–CO)
$S_0 \rightarrow S_3$	1.4893	832.53	0.0001	(HOMO-2) \rightarrow (LUMO)	CT (RuNCS–CO)
$S_0 \rightarrow S_4$	1.5304	810.15	0.0219	(HOMO-1) \rightarrow (LUMO)	CT (RuNCS–CO)
$S_0 \rightarrow S_5$	1.5449	802.53	0.0226	(HOMO-2) \rightarrow (LUMO)	CT (RuNCS–COOH)
$S_0 \rightarrow S_6$	1.6616	746.19	0.0784	(HOMO-1) \rightarrow (LUMO)	CT (RuNCS–COOH)
$S_0 \rightarrow S_7$	2.0312	610.39	0.0300	(HOMO-1) \rightarrow (LUMO+1)	CT (RuNCS–CO)
$S_0 \rightarrow S_8$	2.0454	606.17	0.1013	(HOMO) \rightarrow (LUMO+1)	CT (RuNCS–COOH)
$S_0 \rightarrow S_9$	2.0749	597.53	0.0057	(HOMO-3) \rightarrow (LUMO)	CT (RuNCS–COOH)
$S_0 \rightarrow S_{10}$	2.1626	573.31	0.0615	(HOMO-2) \rightarrow (LUMO+1)	CT (RuNCS–CO)

^a CT: charge transfer.

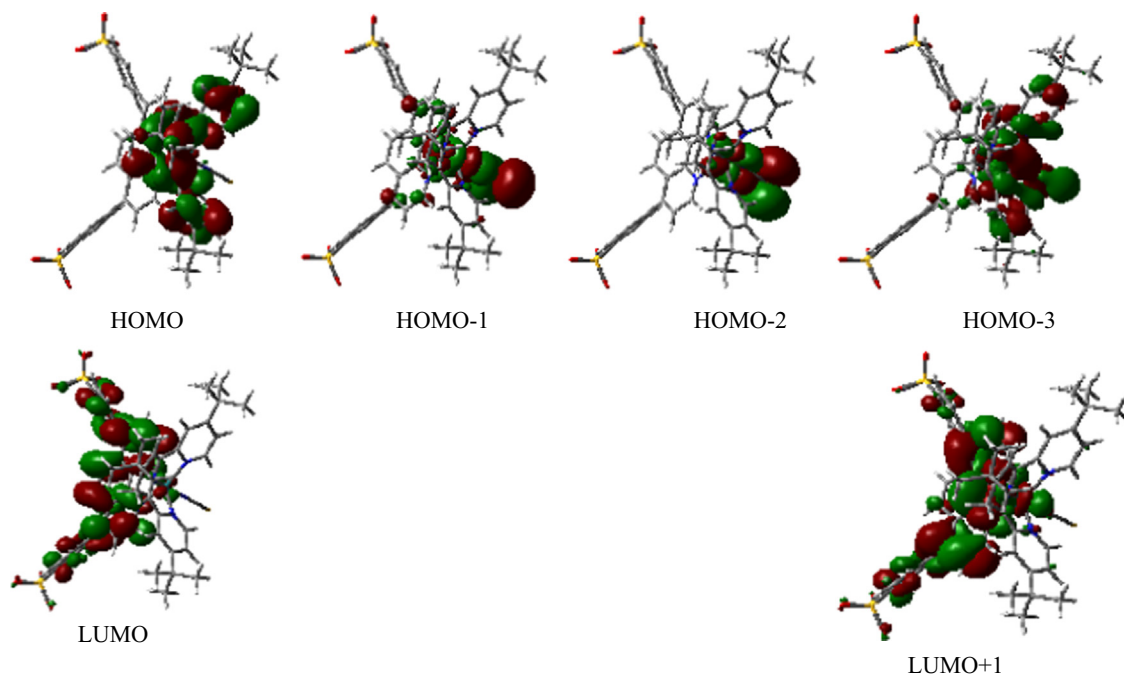


Fig. 9. Schematic representation of the molecular orbitals of K328 obtained from DFT (B3LYP/LANL2DZ) method.

the gas phase. DFT calculations of the compound's ground state indicate that the highest occupied MOs localized on *Ru [tert-butyl-bpy]* groups energetically match the semiconductor valence band; the lowest unoccupied MOs lie above the conduction band edge and are *Ru[phen]* π^* in character. Various excited states of the complex are identified using time-dependent density functional theory (TD-DFT). The TD-DFT calculations revealed that the $S_0 \rightarrow S_1$ transitions for complex are pure charge transfer transitions from donor to acceptor molecules between HOMO and LUMO of the complex.

4. Conclusion

Ruthenium phenanthroline complex shows better efficiencies as a photosensitizer in the TiO_2 based solar cell compared to ZnO ones. Although the sulfonate group did offer stronger binding onto the semiconductor surface, this does not help to improve cell performance for ZnO based solar cells. This situation can be explained by the pH of the solution which affects the surface charge of the semiconductor. As a result of this effect, the complex binding onto the ZnO surface cannot contribute to electron injection efficiently, and this leads to lower electron injection yield for ZnO based DSSC compared to TiO_2 electrodes. We found that electrostatic interactions and the anchoring geometry of the complex on the semiconductor surface determining electron coupling between the complex and semiconductor are important for efficient electron injection.

Acknowledgments

We acknowledge financial support from the Scientific and Technological Research Council of Turkey, TUBITAK

and to Alexander von Humboldt Foundation (AvH). We thank Mechanical Engineer MSc. Cagatay Ela for illustrating figures and his fruitful help.

References

- [1] B. O'Regan, M. Gratzel, *Nature* 353 (1991) 737.
- [2] F.Y. Moussa, Y. Boukennous, A. Elkechai, *Mater. Sci. Semicond. Process.* 16 (2013) 51.
- [3] M. Hamadani, V. Jabbari, A. Gravand, *Mater. Sci. Semicond. Process.* 15 (2012) 371.
- [4] M. Hamadani, A. Gravand, V. Jabbari, *Mater. Sci. Semicond. Process.* 16 (2013) 1352.
- [5] R. Jayakrishnan, S. Gandhi, P. Suratkar, *Mater. Sci. Semicond. Process.* 14 (2011) 223.
- [6] (a) K. Ocakoglu, E. Harputlu, P. Guloglu, S. Erten-Ela, *Inorg. Chem. Commun.* 24 (2012) 118;
(b) S. Erten, E. Eren, S. Icli, *Eur. Phys. J. Appl. Phys.* 38 (2007) 227;
(c) A. Cagatay Cakir, S. Erten-Ela., *Adv. Powder Technol.* 23 (2012) 655.
- [7] S. Wenger, P.A. Bouit, Q. Chen, J. Teuscher, D.D. Censo, R. Humphry-Baker, J.E. Moser, J.L. Delgado, N. Martín, S.M. Zakeeruddin, M. Graetzel, *J. Am. Chem. Soc.* 132 (2010) 5164.
- [8] P.A. Bouit, M. Marszalek, R. Humphry-Baker, R. Viruela, E. Ortí, S.M. Zakeeruddin, M. Graetzel, J.L. Delgado, N. Martín, *Chem. Eur. J.* 18 (2012) 11621.
- [9] A. Reynal, A. Forneli, E. Martinez-Ferrero, A. Sanchez-Diaz, A. Vidal-Ferran, E. Palomares, *Eur. J. Inorg. Chem.* (2008) 1955.
- [10] K. Ocakoglu, C. Zafer, B. Cetinkaya, S. Icli, *Dyes Pigments* 75 (2007) 385–394.
- [11] V.M. Guerin, C. Magne, Th. Pauporté, T. Le Bahers, J. Rathousky, *ACS Appl. Mater. Interfaces* (2) (2010) 3677.
- [12] C. Li, M.Z. Hoffman, *Inorg. Chem.* 37 (1998) 830.
- [13] J.N. Demas, J.W. Addington, S.H. Peterson, E.W. Harris, *J. Phys. Chem.* 81 (1977) 1039.
- [14] A. Hagfeldt, M. Gratzel, *Chem. Rev.* 95 (1995) 49.
- [15] T. Stergiopoulos, S. Karakostas, P. Falaras, *J. Photochem. Photobiol. A* 163 (2004) 331.
- [16] R. Argazzi, C.A. Bignozzi, T.A. Heimer, G.M. Hasselmann, G.J. Meyer, *Inorg. Chem.* 37 (1998) 4533.
- [17] Z. Jin, H. Masuda, N. Yamanaka, M. Minami, T. Nakamura, Y. Nishikitani, *J. Phys. Chem. C* 113 (2009) 2618.

- [18] C.J. Chandler, L.W. Deady, J.A. Reiss, *J. Heterocycl. Chem.* 18 (1981) 599.
- [19] K. Sayama, H. Sugihara, H. Arakawa, *Chem. Mater.* 10 (1998) 3825.
- [20] K. Ocakoglu, S. Sogut, H. Sarica, P. Guloglu, S. Erten-Ela, *Synth. Metals* 174 (2013) 24–32.
- [21] (a) S. Erten-Ela, S. Cogal, S. Icli, *Inorg. Chim. Acta* 362 (2009) 1855;
(b) S. Erten-Ela, S. Cogal, G. Turkmen, S. Icli, *Curr. Appl. Phys.* 10 (2010) 187;
(c) S. Erten-Ela, *International Journal of Photoenergy* 436831 (2013) 1.
- [22] K. Kalyanasundaram, M. Grätzel, *Coord. Chem. Rev.* 177 (1998) 347–414.
- [23] S. Agrawal, N.J. English, K. Ravindranathan Thampi, J.M.D. MacElroy, *Phys. Chem. Chem. Phys.* 14 (2012) 12044–12056.
- [24] K. Rajeshwara, M.E. Osugi, W. Chanmanee, C.R. Chenthamarakshan, M.V.B. Zanoni, P. Kajitvichyanukul, R. Krishnan-Ayer, *J. Photochem. Photobiol. C: Photochem. Rev.* 9 (2008) 171–192.
- [25] F.Y. Qu, P.C. Morais, *J. Chem. Phys.* 111 (1999) 8588–8594.
- [26] G. Ramakrishna, H.N. Ghosh, *Langmuir* 19 (2003) 505–508.
- [27] M.J. Frisch, et al., *Gaussian 03* (2004).
- [28] A.D. Becke, *J. Chem. Phys.* 98 (1993) 5648.
- [29] C. Lee, W. Yang, R.G. Parr, *Phys. Rev. B* 37 (1988) 785.
- [30] P.J. Hay, R.W. Willard, *J. Chem. Phys.* 82 (1985) 270.
- [31] A.D. McLean, G.S. Chandler, *J. Chem. Phys.* 72 (1980) 5639.
- [32] E. Runge, E.K.U. Gross, *Phys. Rev. Lett.* 52 (1984) 997.